



## Article

# Analysis of Temporal and Spatial Variability of Fronts on the Amery Ice Shelf Automatically Detected Using Sentinel-1 SAR Data

Tingting Zhu <sup>1,†</sup>, Xiangbin Cui <sup>2,†</sup> and Yu Zhang <sup>3,\*</sup>

<sup>1</sup> State Key Laboratory of Information Engineering in Surveying, Mapping and Remote Sensing, Wuhan University, Wuhan 430079, China; ztt\_polar\_rs@whu.edu.cn

<sup>2</sup> Polar Research Institute of China, Shanghai 200136, China; cuixiangbin@pric.org.cn

<sup>3</sup> Chinese Antarctic Center of Surveying and Mapping, Wuhan University, Wuhan 430079, China

\* Correspondence: yuzhang\_spl@whu.edu.cn

† These authors contributed equally to this work.

**Abstract:** The Amery Ice Shelf (AIS) dynamics and mass balance caused by iceberg calving and basal melting are significant in the ocean climate system. Using satellite imagery from Sentinel-1 SAR, we monitored the temporal and spatial variability of the frontal positions on the Amery Ice Shelf, Antarctica, from 2015 to 2021. In this paper, we propose an automatic algorithm based on the SO-CFAR strategy and a profile cumulative method for frontal line extraction. To improve the accuracy of the extracted frontal lines, we developed a framework combining the Constant False Alarm Rate (CFAR) and morphological image-processing strategies. A visual comparison between the proposed algorithm and state-of-the-art algorithm shows that our algorithm is effective in these cases including rifts, icebergs, and crevasses as well as ice-shelf surface structures. We present a detailed analysis of the temporal and spatial variability of fronts on AIS that we find, an advance of the AIS frontal line before the D28 calving event, and a continuous advance after the event. The study reveals that the AIS extent has been advanced at the rate of 1015 m/year. Studies have shown that the frontal location of AIS has continuously expanded. From March 2015 to May 2021, the frontal location of AIS expanded by 6.5 km; while the length of the AIS frontal line is relatively different after the D28 event, the length of the frontal line increased by about 7.5% during 2015 and 2021 (255.03 km increased to 273.5 km). We found a substantial increase in summer advance rates and a decrease in winter advance rates with the seasonal characteristics. We found this variability of the AIS frontal line to be in good agreement with the ice flow velocity.

**Keywords:** frontal position; constant false alarm rate; Sentinel-1 SAR data; Amery Ice Shelf; iceberg calving



**Citation:** Zhu, T.; Cui, X.; Zhang, Y. Analysis of Temporal and Spatial Variability of Fronts on the Amery Ice Shelf Automatically Detected Using Sentinel-1 SAR Data. *Remote Sens.* **2021**, *13*, 3528. <https://doi.org/10.3390/rs13173528>

Academic Editor:  
Nereida Rodriguez-Alvarez

Received: 7 July 2021

Accepted: 1 September 2021

Published: 5 September 2021

**Publisher's Note:** MDPI stays neutral with regard to jurisdictional claims in published maps and institutional affiliations.



**Copyright:** © 2021 by the authors. Licensee MDPI, Basel, Switzerland. This article is an open access article distributed under the terms and conditions of the Creative Commons Attribution (CC BY) license (<https://creativecommons.org/licenses/by/4.0/>).

## 1. Introduction

The fronts of ice shelves in Antarctica are critical interfaces, between the ice sheet and ocean, and their geometry and variation can significantly impact the ice shelf-ocean interaction (e.g., basal melting, and iceberg calving), which further affects upstream ice sheet dynamics and sea-level rise [1]. In September 2019, the Amery Ice Shelf (AIS) calved a 1636-km<sup>2</sup> iceberg named D28. The last major calving event from AIS was in the early 1960s. After the D28 detachment, the mass loss of AIS was approximately 315 billion tonnes due to the iceberg calving at the front, which, in addition to the basal melting underneath, is the key mass loss process. An AIS front advance will increase stress at the rift [2]. Before the D28 detachment, five rifts were actively propagated near the AIS front among seven active rifts over the 13 ice shelves in Antarctica, where most active rifts were initiated at the Amery Ice Shelf fronts [3–5]. Although ice-shelf calving does not influence the global sea level, the location of ice-shelf fronts is an important parameter of ice-sheet dynamics,

which contributes to sea-level rise [6–11]. Moreover, the tabular iceberg (D28) has to be monitored and tracked since the Chinese Antarctic Zhongshan Station, Russian Progress Station and Indian Bharati Station are near the AIS where the D28 broke off may cause shipping hazards. Sentinel-1's fine spatial resolution with 40 m and high repeat acquisitions have allowed for monthly D28 events or daily analysis of the rifts to change the detection and ice fronts dynamic in AIS, the third largest ice shelf in the east of Antarctica and one of the largest glacier drainage basins.

Although attempts have been made to survey the front of AIS through airborne instruments [12], remote satellite sensors can provide continuous measurements for the early detection of ice-shelf calving and fronts dynamics in remote locations as well as can monitor extreme climate conditions due to its remote location, snow, and ice-covered surface, and extremely cold and windy weather conditions [13–15]. The advance or retreat of ice-shelf fronts can be delineated by synthetic aperture radar (SAR) based on its all-weather and frequent repeat observation capabilities, because the microwave can penetrate thick clouds and darkness in polar regions, indicating that SAR may be the most advanced method for monitoring large-scale dynamics in ice-shelf fronts [8,16]. The current generation of SAR satellites including RADARSAT-2 and Sentinel-1 can provide high spatial resolution images with less than 40 m and high temporal availability within one day. High spatial resolution SAR images are easily acquired as open-source data since Sentinel-1 was launched in early 2014. Free Sentinel-1 SAR data access facilitates the possibility of providing long-term satellite observations for the location of ice-shelf fronts and glaciers.

Perennial sea ice or fast ice (sea ice “fastened” to land and motionless with tides) might appear quite similar to shelf ice in remote sensing imagery. Separation of them is a challenging task due to changing sea ice conditions and is our focus in this study. The main goal in this study is to automatically detect the calving frontal dynamics on Sentinel-1 SAR imagery because the manual delineation of calving fronts from remote sensing imagery is extremely time-consuming. The Radarsat-1 Antarctica Mapping Project (RAMP) Antarctic Mapping Mission 1 (AMM) was used to classify the coastline of Antarctica in terms of surface structure patterns is close to the calving front. Mapping and classification for calving fronts of Antarctica based on the automated edge detection method were complemented by manual control [17]. The semi-automated detection method for glacier and ice shelf fronts from Sentinel-1 imagery was proposed based on deep learning technology, which requires enormous training samples [18].

The unsupervised method mostly attempts to focus on the edge detection method for Greenland using MODIS data, such as Sobel, by selecting the peak backscattering value along the direction of ice flow as the ice frontal points [19,20]. Limited by MODIS due to illumination or contamination by clouds, coastline products are incomplete [14]. Continuous observations can be achieved by SAR technology. Using Radarsat-1 SAR data, the coastline is extracted based on a locally adaptive threshold algorithm [21–23], which significantly removes the burden of conventional manual delineation methods. Outcrop rock, surface melting, crevasses, and rifts may cause large computation costs and inaccuracies. A thorough investigation of AIS is required as all of the aforementioned algorithms focus on the continental scale. Our work was inspired by the profile method proposed in [24,25], where the standard deviation (STD) and five-maximum value extraction algorithms were proposed. SAR data with speckle noise, high interclass, and high intraclass backscatter variability degrade the image details and decrease the separability among ocean, coastal rock outcrops, sea ice, and ice shelf. Considering these characteristics, we proposed a framework combining the Constant False Alarm Rate (CFAR) and profile method to automatically detect the ice-shelf fronts in AIS by Sentinel-1 SAR data. To deal with the problem caused by surface structures as well as rifts on the ice shelf and floating ice, the maximum cumulative value-based approach is used to find the frontal points of each profile. A morphological filter is then used to remove the icebergs. Finally, the time series of the frontal position displacement, as well as the regional dynamic of the ice shelf, is investigated.

In this work, following an overview of the scientific motivations and the Sentinel-1 SAR data used on AIS in Section 1, Section 2 comprises the methodology for the determination of glacier front location fields, with a focus on the proposed detection framework. Subsequently, the results of the AIS front location and analysis of more than seven-years-time series (2015–2021) for their dynamics are presented in Section 3. Section 3 also discusses the AIS D28 calving event. Conclusions are given in Section 4.

## 2. Methods

The frontal line extraction algorithm consists of three steps: SO (Smallest of)-CFAR for binary classification [26–29], morphological image processing [30,31], and maximal cumulative based frontal point extraction [32]. CFAR detectors are adaptable threshold detectors that use various statistical models to detect target returns from the ice shelf against the background clutter, such as sea ice and ocean. The threshold for every detecting cell (sliding window) is adaptive to maintain a constant probability of a false alarm (PFA) according to an assumed background probability density function  $f(x)$ . The sliding window strategies include cell averaging, greatest and smallest of CFAR named as CA-CFAR, GO-CFAR, and SO-CFAR. We use the SO-CFAR strategy combined with Weibull statistical distribution since this strategy can maximize the  $f(x)$  on SAR image in this paper. Afterward, SO-CFAR is used to obtain the binary image. To remove the icebergs on the binary image after CFAR, we use morphological image processing such as opening and closing to remove small fragments. The maximal cumulative value-based method is a strategy designed for frontal point extraction. In this step, we firstly constrain the ice shelf in the defined borders region. Between two borders of the ice shelf, the longitudinal profiles are generated by an equal divide. Then, the frontal points are determined by the cumulative maximal values. Finally, the frontal lines can be automatically delineated. The detailed flowchart is illustrated in Figure 1.

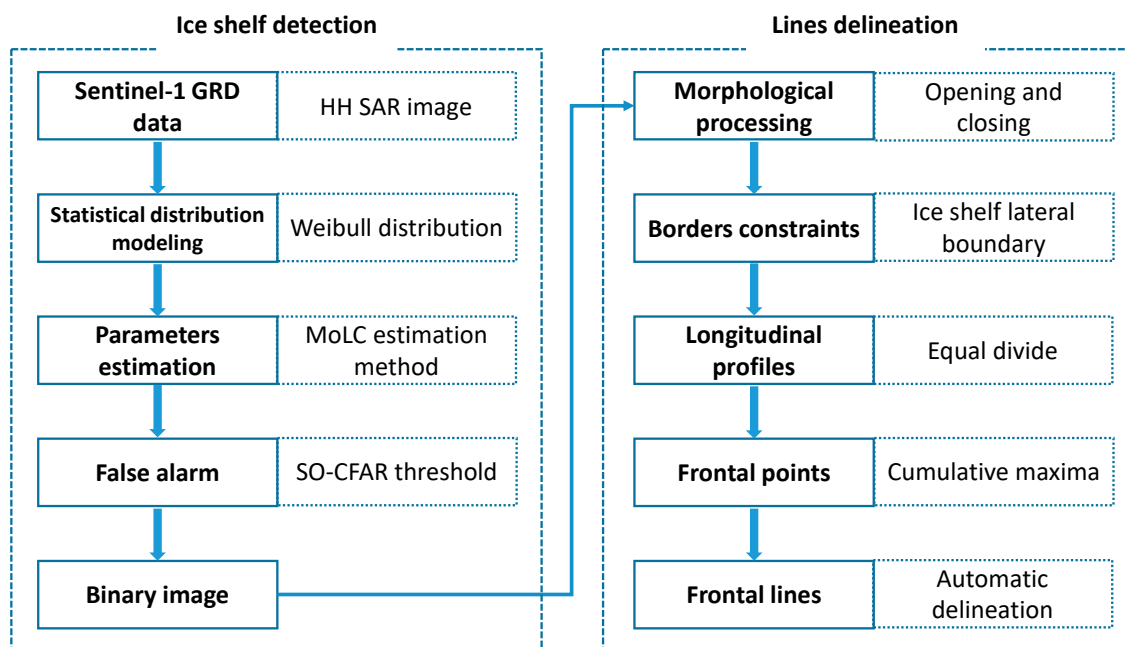


**Figure 1.** Flowchart of the frontal lines detection algorithm. The left panel is for the ice shelf detection and the right panel is for delineating frontal lines.

### 2.1. Ice shelf Detection Using CFAR Method

The ice-shelf areas in Sentinel-1 SAR imagery can be detected using the CFAR method [26]. For CFAR modeling, we first model the distribution of the SAR backscatter using Weibull distribution since it is suitable for ocean and ice clutter modeling [27]. Then, the CFAR method

is carried out based on a constant false alarm rate to identify the SAR pixel as the ice shelf label. To classify the SAR image into the ice shelf label and the background label, a SO-CFAR based detection approach is used [33,34]. For a given pixel in SAR imagery, we first select a clutter region with a window size of  $(2n + 1)$ . We define the guard area with sizes of  $(2m + 1)$  as the test cell. Except for the guard area, the remaining pixels are equally divided into two parts: P1 and P2 with the size of  $(n-m)$ . The SO-CFAR strategy selects the minimum value P of P1 and P2, where P1 and P2 are the mean values of the sum intensity (mean power) of the local clutter region. Then, pixels in the clutter regions are compared with P, and pixels larger than P are selected for Weibull modeling. In this paper, the Weibull distribution-based SO-CFAR method is used to detect the ice shelf pixel in the SAR imagery. Then, the adaptive threshold for the pixel is calculated using the SO-CFAR strategy. Finally, if the intensity of the given pixel is larger than the threshold  $T$ , it will be labeled as an ice shelf with the value 1; otherwise, it is labeled as the background (clutter) with a value of  $-1$ . A detailed flowchart for the SO-CFAR method is illustrated in Figure 2.

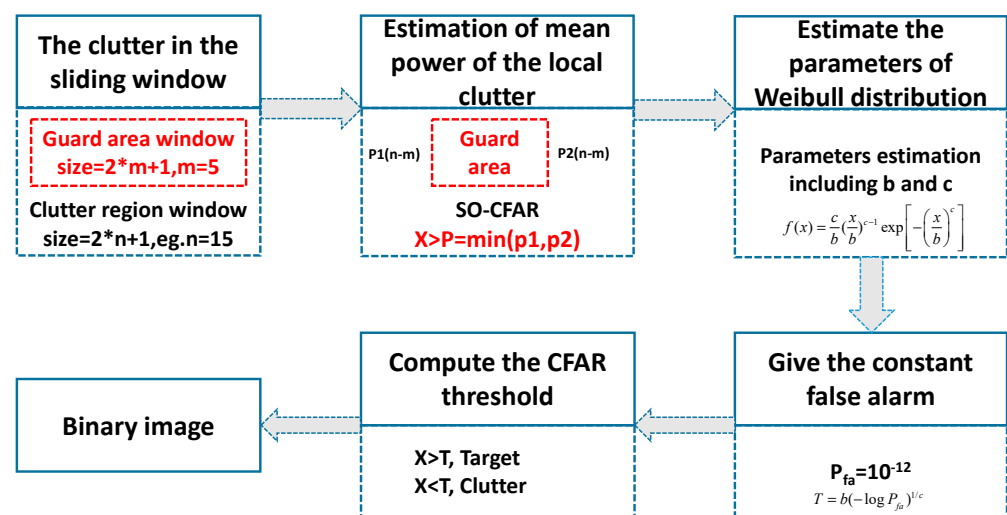


Figure 2. Flowchart of the SO-CFAR method for ice shelf detection.

The following is the formula for CFAR threshold:

$$1 - P_{fa} = \int_0^T f(x) dx, \quad (1)$$

where  $f(x)$  is the probability density function and we use Weibull distribution to modify the distribution of SAR clutter.  $x$  is the intensity value of SAR imagery, and  $P_{fa}$  is the given false alarm rate. We assume the clutter following the Weibull model taking the probability density functions (PDF) form:

$$f(x) = \frac{c}{b} \left(\frac{x}{b}\right)^{c-1} \exp\left[-\left(\frac{x}{b}\right)^c\right] \quad (2)$$

where  $b$  and  $c$  are the scale and shape parameters, respectively, and are estimated by the method of logarithmic cumulants (MoLC) parameter estimation approach [35].  $T$  can be obtained after  $b$  and  $c$  calculation using the following formula:

$$T = b(-\log P_{fa})^{1/c}, \quad (3)$$

In this study, the false alarm rate  $P_{fa}$  is set to  $10^{-12}$  and the threshold is calculated automatically within the given sliding window. Pixels in the sliding window are compared with the threshold  $T$ , and those larger than the threshold are treated as the ice shelf;

otherwise, they are treated as the background. Then, the binary image is automatically obtained by the adaptive threshold from the SO-CFAR method for the following processing.

As glacier and ice-shelf fronts are dynamic due to calving events, there are a large number of disintegrating icebergs in the front of the ice shelf, as can be seen on the binary imagery from SO-CFAR results. The presence of rifts, pressure ridges, crevasses, and depressions on ice-shelf surfaces may be mistakenly detected as the background on SO-CFAR binary imagery. The heterogeneous characteristics of SAR backscatter on ice-shelf surfaces may cause significant uncertainties for the following profile processing. Therefore, a post-processing step is required for an SO-CFAR binary image to remove some floating icebergs and to fill in gaps resulting from heterogeneous ice surfaces, since it may affect the accuracy of ice-shelf front point extraction. To solve these problems, a morphological filter sequence including opening and closing is exploited [36]. The morphological opening is used to dilate an eroded image to remove isolate bright structures such as the floating icebergs. Morphological closing is used to erode a dilated image to suppress dark holes such as the heterogeneous ice surface structures. In this paper, a combination of opening and closing filters with a window size of  $5 \times 5$  pixels can obtain the optimal result using SO-CFAR for ice shelf point extraction.

## 2.2. Profile Analysis Based Frontal Point Extraction

The accuracy of ice-shelf extraction is affected by the ice spatial distribution in the frontal area, where there is some floating sea ice in front of the ice shelf. The fraction of floating iceberg also decreases the accuracy of the traditional algorithm for frontal position detection. For the ice shelf frontal point extraction, the real condition of the ice-shelf frontal area can be treated as the following three situations shown in Figure 3. Two red lines were manually labeled as shown in Figure 3, which define the border area for the AIS. The three purple lines L1-L3 show the different ice conditions in the frontal area, where the most common case L3 means that there is no obstacle in the frontal area. From 22 to 25 September 2019, a huge iceberg named D28 was breaking off from AIS, and there was a large amount of floating iceberg in the frontal position area of L1 and L2. L2 means that the profile line only crosses a small piece of iceberg. L1 shows that the profile line penetrates the main body of the D28 iceberg even though the morphological operation is used after CFAR detection, and L2 means that the profile line only crosses a small piece of the iceberg. To give a brief description of the frontal points extraction in this study, the distribution of ice-shelf points on Sentinel-1 SAR imagery and the corresponding cumulative value for the three conditions are illustrated in Figure 3.

The cumulative value beginning from the original to  $k$  position along the defined profile is  $value(K)$ .  $Diff_{Buffer}(k, n)$  is the minus of cumulative values at  $k$  and  $n$ . For L2 and L3 in Figure 3d,e, the frontal point detection is treated as extracting the position along each profile, where the cumulative value  $value(K)$  at position  $K$  (Equation (4)) along the current profile reaches the peak, and  $L(i)$  is 1 for the ice shelf and  $-1$  for the background. For the L3 profile, the peak value appears on the end area of the floating ice along the profile. To detect the real location of the ice-shelf frontal point, we first define a buffer area with the length of  $n$  along the given profile. If the difference of the cumulative value  $Diff_{Buffer}(k, n)$  is  $-n$ , then the position in the buffer area is the final frontal point of the ice shelf. In this paper, the length of buffer area  $n$  is set to 5, which equals 200 m with the pixel spacing of 40 m for Sentinel-1 SAR imagery. The new filter is also suitable for the L1 and L2 cases, and it will be used as the criterion for frontal point extraction in all profiles.

$$value(K) = \sum_{k=1}^K L(i) \quad (4)$$

$$Diff_{Buffer}(k, n) = value(k) - value(k - n) \quad (5)$$

The Sentinel-1 imagery was preprocessed using the Python toolbox and the extraction of the regions was performed by the ArcGIS software package. The SO-CFAR and morphological algorithms were executed on the MATLAB 2019b platform.

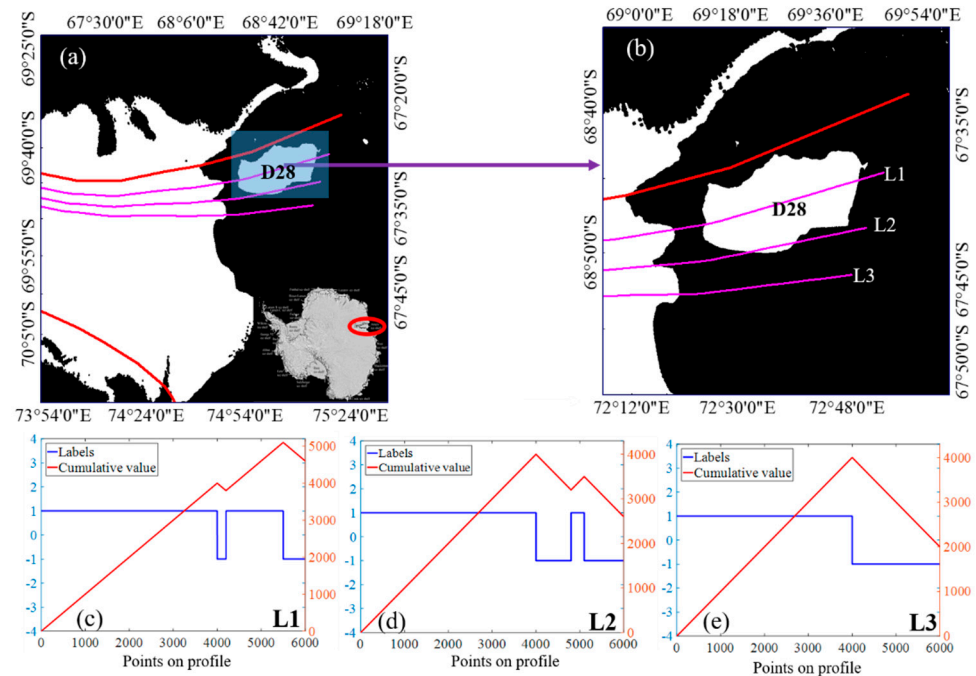


**Figure 3.** Frontal points extraction criterion for different ice conditions. In (a,b), the red line is the boundary we defined in this study and the magenta is the defined profile line. Figures (c–e) illustrate the cumulative values for three different situations for frontal points extraction. (c) it means profiles cross the main body of floating ice. (d) it means profiles cross a small part of floating ice. (e) it means no floating ice along the profile.

### 3. Results and Discussion

The Global Monitoring for Environment and Security (GMES) programme led by the European Space Agency (ESA), which has operated the Sentinel-1 mission with free and open data access, is suitable for ice monitoring. For this purpose, Sentinel-1A/B was launched in April 2014 and August 2016, respectively, providing a near-polar, sun-synchronous orbit with a 6-day repeat time. The C-band Sentinel-1 SAR image with a high spatial resolution of 40 m contains much more detailed information with four modes: stripmap (SM), wave (WV), interferometric wide swath (IW), and extra-wide swath (EW). Due to the all-day and all-weather capabilities of Sentinel-1, it has been widely used and has demonstrated its potential in cryosphere observation [37]. We delineated the defined boundary of AIS as the study area with the red line and the profile (green line) shown in Figure 4. In Figure 4, we first provide details on the study sites and dataset selected for the temporal and spatial variability of fronts on the AIS.

In this paper, Sentinel-1 level 1 Ground Range Detected (GRD) SAR scenes between 2015 and 2021 are downloaded from the ESA Scientific Data Hub (<https://scihub.copernicus.eu/>). We used single polarization in the HH channel with EW mode and with a spatial resolution of 40 m in the range and azimuth direction, respectively, for extracting the front position of AIS. The swath width of the SAR image is 500 km with the incidence angle ranging from 18.3° to 46.8°. We calculated the monthly frontal position extension on AIS during the observation period using the proposed algorithm (Figure 4). For each month, more than one image is available while we only select one scene for monitoring the AIS frontal position, as shown in the right panel of Figure 4. As can be seen, a total of 75 Sentinel-1 image products were selected for ice fronts extraction. To show the general trend of annual ice fronts, we use a different color for the annual AIS front position, which

shows the general advance during the observing period and regional retreat due to the D28 calving event. In addition, for further analysis of the D28 iceberg calving cases, we use the acquisitions between 18 September 2019 and 31 October for a total of 14 Sentinel-1 images. We follow with a discussion of the details for the AIS frontal position and the three special calving cases in the defined regions, as shown in Figure 4.

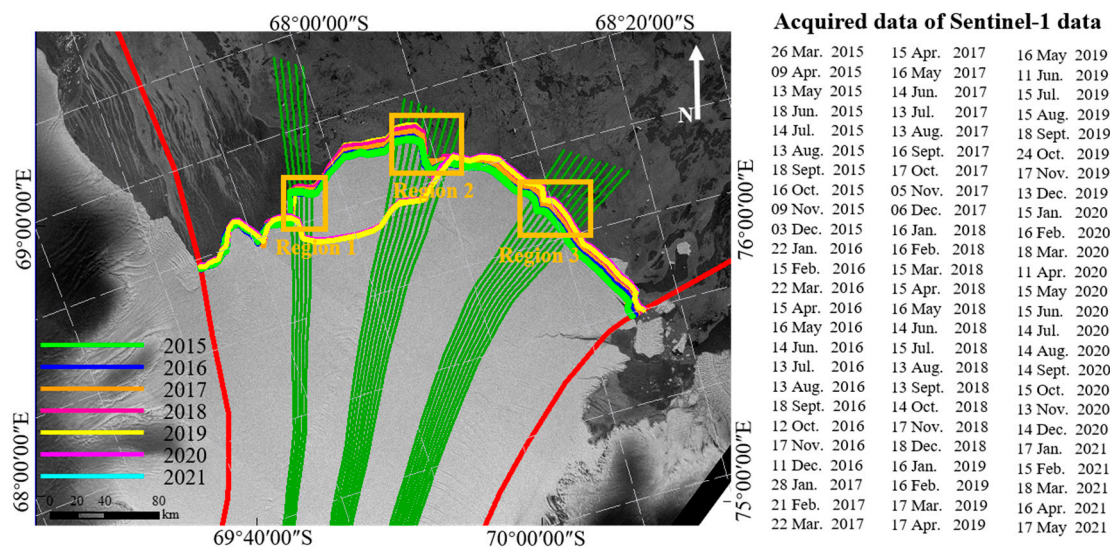


**Figure 4.** Research area and data set used in this study. The general trend of ice frontal position between 2015 and 2021 for Amery Ice Shelf. The colors indicate the time difference. We defined three regions for dynamical and seasonal analysis. The right panel is the data used for the spatio-temporal analysis. The background is from single-polarized Sentinel-1 data accessed on 26 March 2015.

### 3.1. Visual Performance and Comparison of Ice-Shelf Frontal Point Extraction

To improve the visual performance of frontal point extraction, we proposed the strategy that SO-CFAR is used for the binary ice-shelf classification. We extracted the frontal position of AIS from 2015 to 2021. The ice-shelf frontal line extraction algorithm is validated by comparison with the state-of-the-art approach on three situations, including the rifts, calving iceberg as well as visible surface structures (e.g., the crevasse and pressure ridges). To show the visual performance of the proposed frontal line extraction method, three sample Sentinel-1 SAR images acquired on 26 March 2015, 24 October 2019, and 22 September 2019 are presented in Figure 5. As can be seen in Figure 5a–c, we show the results from our algorithm (upper) and the comparison algorithm (bottom) in [27] in terms of rift, calving icebergs, and surface features, respectively. The comparison algorithm mainly utilizes the statistics of backscattering values and maximal values to decide the frontal position. As shown in Figure 5a, the profile line has more than one intersection of frontal points while the comparison algorithm can only provide one frontal point. Our algorithm has good performance due to the strategy of firstly using the CFAR algorithm to detect the ice shelf. Especially in the calving iceberg case, the profile for the comparison algorithm is ineffective since the frontal points are on the floating iceberg, which is close to the ice shelf. This is because the proposed algorithm utilizes the morphological filter to remove the isolated icebergs. Although the comparison algorithm is not effective in these above-mentioned cases, it has provided new insight for us to propose a new strategy based on this framework.

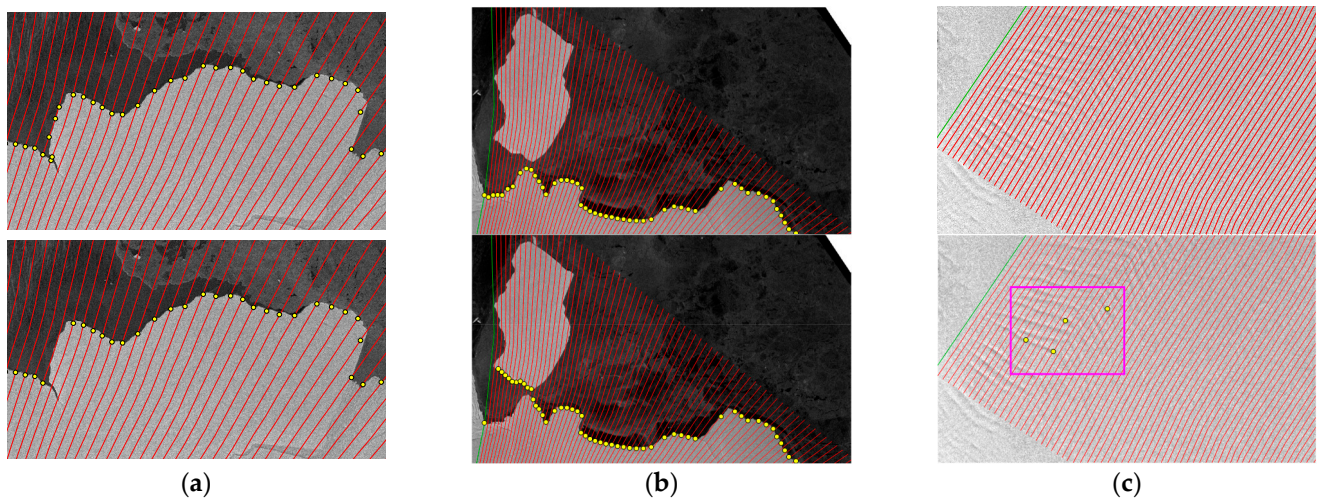


**Figure 5.** Frontal point extraction on sample Sentinel-1 SAR images using the proposed algorithm (upper) and the comparison method (bottom). (a) 26 March 2015; (b) 24 October 2019; (c) 22 September 2015.

### 3.2. Spatio-Temporal Changes in the Ice-Shelf Frontal Line from 2015 to 2021

In addition to the visual performance with the state-of-the-art algorithm, we use the manual delineation of the frontal line in three regions to evaluate the proposed algorithm, and their accuracies report is given in Table 1. In this time span, we select seven datasets in March of each year to quantify their accuracies. The proposed algorithm is superior to the comparison method especially in Region 1 and Region 2, where the bias of the averaged distance compared with reference frontal line using the proposed algorithm is smaller than the comparison approach, especially in Region 1 and Region 2 area. This is because the frontal line in Region 1 and Region 2 is much more complicated than that in Region 3 with regard to some rifts, indicating that our algorithm can deal with more complex cases.

**Table 1.** Validation of frontal line extraction using different methods.

Date	Average Distance of Frontal Position Compared with Reference Frontal Line [m]					
	Region 1		Region 2		Region 3	
	Proposed	Comparison	Proposed	Comparison	Proposed	Comparison
2015-03-26	26.44	156.34	38.23	145.21	12.33	33.21
2016-03-22	28.32	143.25	44.21	165.36	9.24	32.55
2017-03-22	22.07	166.57	39.56	165.33	8.75	27.88
2018-03-15	26.33	124.32	45.12	154.06	13.65	24.35
2019-03-17	26.21	156.36	40.55	168.31	7.88	30.22
2020-03-18	23.21	137.45	35.66	144.23	10.44	25.48
2021-03-18	24.83	147.06	37.23	135.23	8.75	27.01

The time-series results of the terminus on the AIS as shown in Figure 6a indicate that the front of the AIS has an advancing trend of outward expansion between 2015 and 2021. In September 2019, an area of about 1600 km<sup>2</sup> of the iceberg D28 detached from the Amery Ice Shelf, which caused the AIS front to retreat instantaneously. The advance displacement of AIS fronts from March 2015 to September 2019 in Figure 6a shows that the total displacement over these five-year periods was 4650 m, with the slope for each year meaning the monthly change rate. A significant expanding tendency of frontal position from 2015 to 2018 is clearly seen. While in 2019, the displacement rate retreated by 280 m after the D28 calving. During the iceberg calving, the frontal line has retreated by an average of 280 m shown in Figure 6b. From 2019 to 2021, the overall advance was an approximate 2.05 km extension. After the D28 event, the ice shelf continued to

expand outward. Until May 2021, the overall expansion distance of the terminus of the AIS expanded by approximately 6500 m compared with that in March 2015. After the D28 detachment, the AIS was with 273.5 km of frontal lines compared with 255.03 km in March 2015 although the frontal points were advanced. From 2015 to 2021, the length of fronts is increased by 7.5%. During the D28 event, the length of frontal lines of the AIS suddenly increased (Figure 6b), and then the length of the frontal line remained unchanged. However, the frontal points keep expanding as can be seen in Figure 6a.

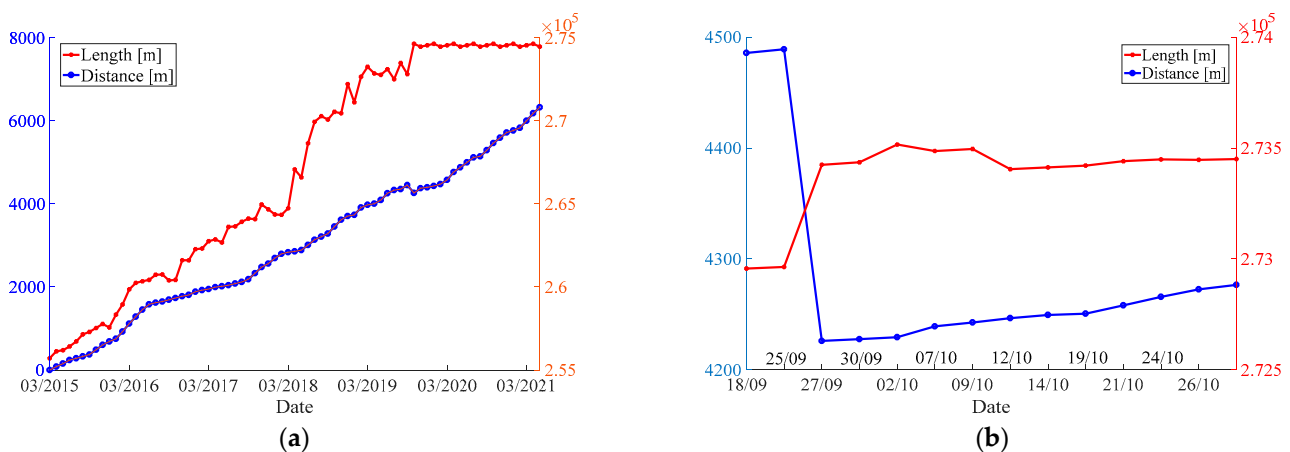


**Figure 6.** Time series variability in frontal lines of the AIS monitored during March 2015–May 2021. Relative changes in frontal lines of the AIS during the D28 calving event in September 2019. The length and extension distance are coded as shown. (a) Monthly cumulative extension distance and length of frontal line for the AIS from 2015 to 2021; (b) cumulative extension distance and length of frontal line for the AIS during the D28 calving event.

The length of AIS fronts has also shown an increasing trend since 2015, and from the beginning of 2018 to September 2019, the length of the AIS front shows a clear advancing trend. It is worth noting that the rapidly increasing rate between January 2018 and September 2019 is the reason for the D28 iceberg calving; the main reason may be due to the intensified ice-shelf activity. We show the length of the rift in Region 2 in Figure 7. As can be seen in Figure 7, the rift in Region 2 is becoming wider and wider. The wider rifts led to longer fronts. The AIS front intensifies its advance between March 2018 and October 2018 and increased the stress on the rifts especially in region 2 which accelerated the D28 calving. The advance during this period can be attributed to the ice velocity, which is discussed in the next section. Figure 6b shows the time series results during the disintegration of D28. The D28 iceberg disintegration event can also be seen as having occurred from 25 September to 27 September 2019.

The advance and retreat of AIS were assessed using Sentinel-1 images during 2015 and 2021. The time series of visual results for the three regions from 2015 to 2021 are shown in Figure 6. The general trend for retreat or advance is shown in Figure 4. In the experiment, the ice-shelf frontal line extraction algorithm is validated by visual comparison with the state-of-the-art approach, where the spatial and temporal dynamics of AIS in three defined regions is discussed. In this section, Regions 1 and 2 are used to show the dynamic change of frontal lines in detail including the D28 calving event. Region 1 is located in the west of the AIS and as can be seen in Figure 8a, the profile (green line) has multiple intersections with AIS fronts. The proposed method can successfully detect all the frontal points in the profile, which can provide an accurate frontal line. In September 2019, the D28 iceberg broke up from Region 1 and Region 2, which led to a large amount of floating ice in the front of AIS. The proposed method can also suppress the influence of large floating ice in the front of the AIS. After the D28 event, we can see the obvious retreat of the frontal lines in Region 1. With respect to Region 2 located in the middle of the AIS, the retreat occurred at the rifting area while the advance is continuous in Region 3. Due to iceberg calving,

we can find a significant dynamic of the frontal position in Region 1 and Region 2, while Region 3 shows a stable expansion pattern.

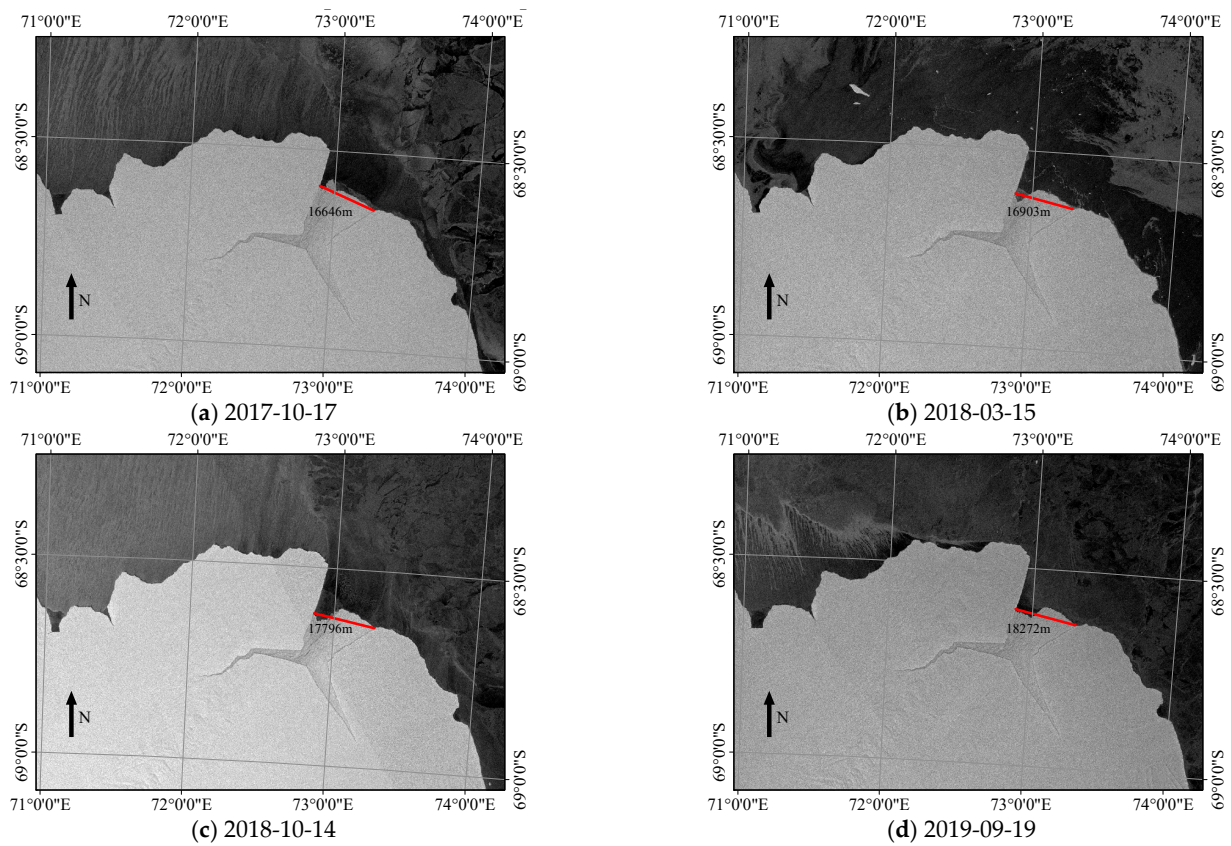


**Figure 7.** The advanced AIS fronts from March 2018. The rift in Region 2 became wider and wider. The length of the rift is marked in the respective panel.

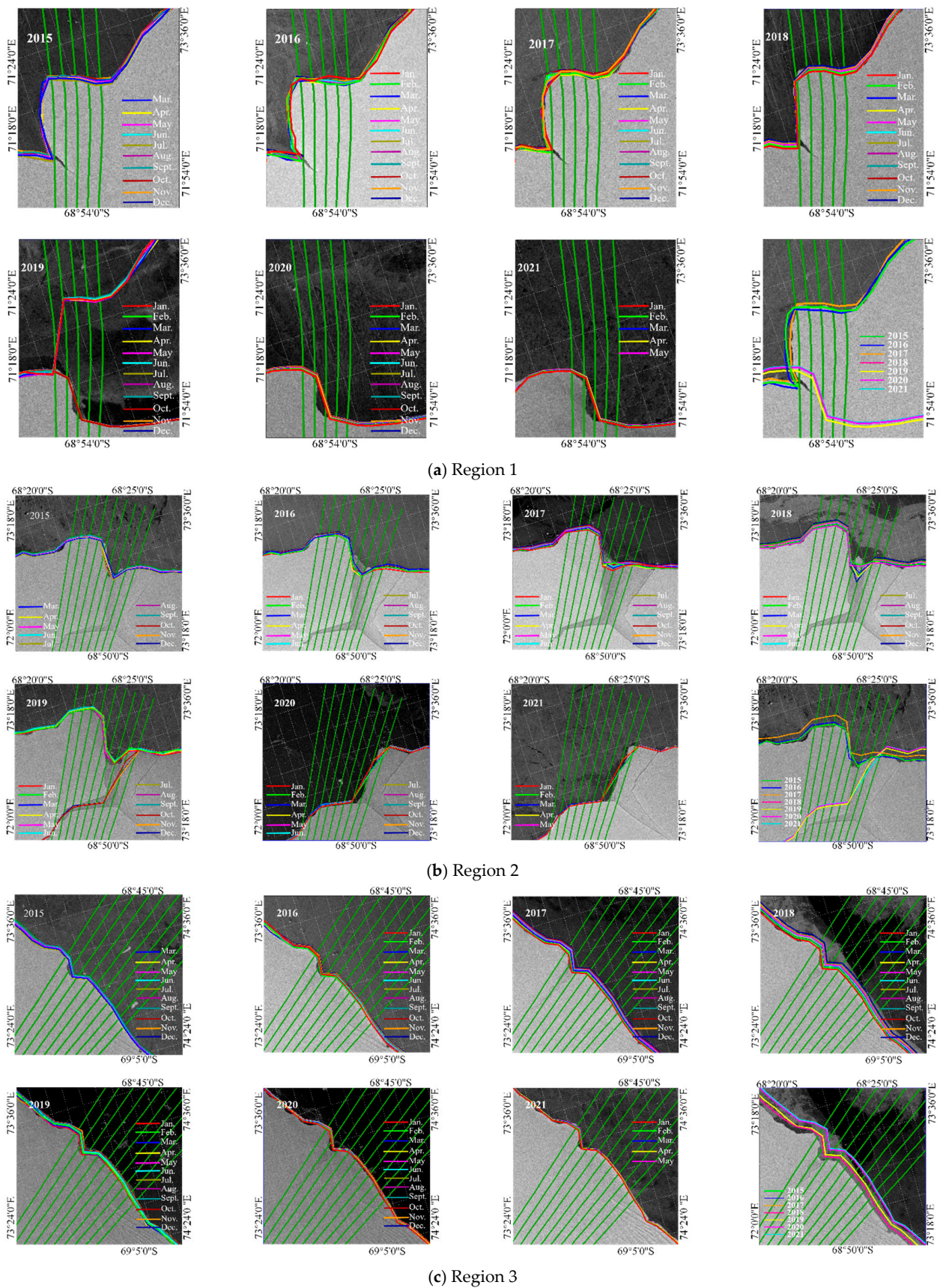


**Figure 8.** The result of frontal line in the three regions from 2015 to 2021. All the background image is acquired in March of each year except for 2019 in September. For the last panel, the background image were acquired in March 2015 for Region 1, 2, and 3. (a) Region 1; (b) Region 2; (c) Region 3.

With respect to Region 1 and Region 2, Region 3 is much more stable. We compared the seasonal dynamics in Region 3 using the monthly average extension distance shown in Figure 9, where it is clear that the frontal position of the AIS has a significant seasonal trend. Compared with the expansion speed from October to March and April to September in Region 3, the AIS frontal position shows a relatively faster speed in the austral summer seasons compared to the austral winter. During 2016–2020, the average monthly expansion distance from January to April gradually decreases, and it starts to increase from April. The maximal average monthly expansion distance appeared in October with the expansion distance larger than 130 m in 2018. During the summer season, the speed of ice flow on the AIS increased, which is the main reason for the acceleration of frontal position expansion. For the annual variance from April to October, the expansion speed is accelerating, the expansion speed reaching the top in October 2018 before the D28 event.

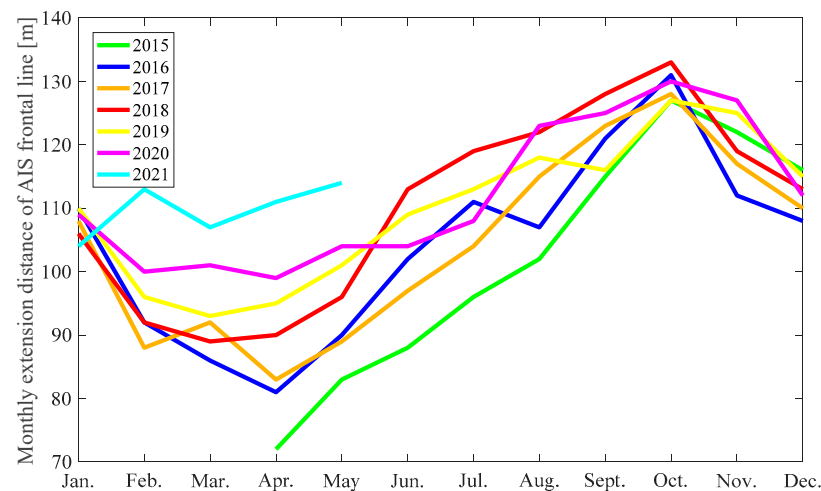


**Figure 9.** Seasonal advance rate with the expansion distance of the AIS frontal line in Region 3. The monthly average advance rate for each year is color-coded.

### 3.3. Ice Velocity

To validate the accuracy of the displacement retrieved using the proposed method, the ice velocity product from 2015–2016, provided by [37,38], is used. We first use 66 matched points to generate the scatter plot between the proposed result and the MEaSURES ice velocity product in Figure 10a; the standard deviation is 165 m/yr, which means the daily difference for these two results is less than 0.5 m. Moreover, for the relatively stable area in the central and western parts of the AIS, we selected 38 from the 66 points to analyze the linear relationship between these two products. The scatter plot in Figure 10e shows that the standard deviation is 111 m, with a daily bias of 0.3 m. The comparison with the ice velocity dataset indicates that the displacement of the frontal position can also be used to analyze the dynamics of the AIS. Figure 10 shows the correlation analysis between the AIS extended distance and MEaSURES ice velocity products [33,34]. As can be seen from the ice velocity diagram in the above figure, the maximum ice velocity of the AIS ice shelf is mainly concentrated at the intersection of Lambert Glacier (LG), Fisher Glacier (FG), and Mellor Glacier (MG) shown in Figure 10b and at the frontal position area shown in Figure 10c, the maximum ice velocity is about 4.3 m/day. In Figure 10d,e, a scatter plot of the expansion rate of the glacier frontal area and its corresponding ice velocity is presented. Among them, the left picture contains 66 points, which are distributed in the frontal area of the AIS. It can be seen from the picture that the difference between the two data sets of most points is within 200 m/yr, and that the maximum error is about 400 m/yr and that  $R^2$  is 0.88, indicating that there is good consistency between the ice velocity and expansion rate. The scatter diagram on the right contains 38 points, which are distributed in the front area of D28 iceberg disintegration. It can be seen from the figure that the errors of all points are within 300 m/yr, and  $R^2$  is 0.91. The ice velocity in this area is slightly

greater than the expansion rate of the ice shelf, which also caused the area to be active and eventually led to the breakup of the iceberg.

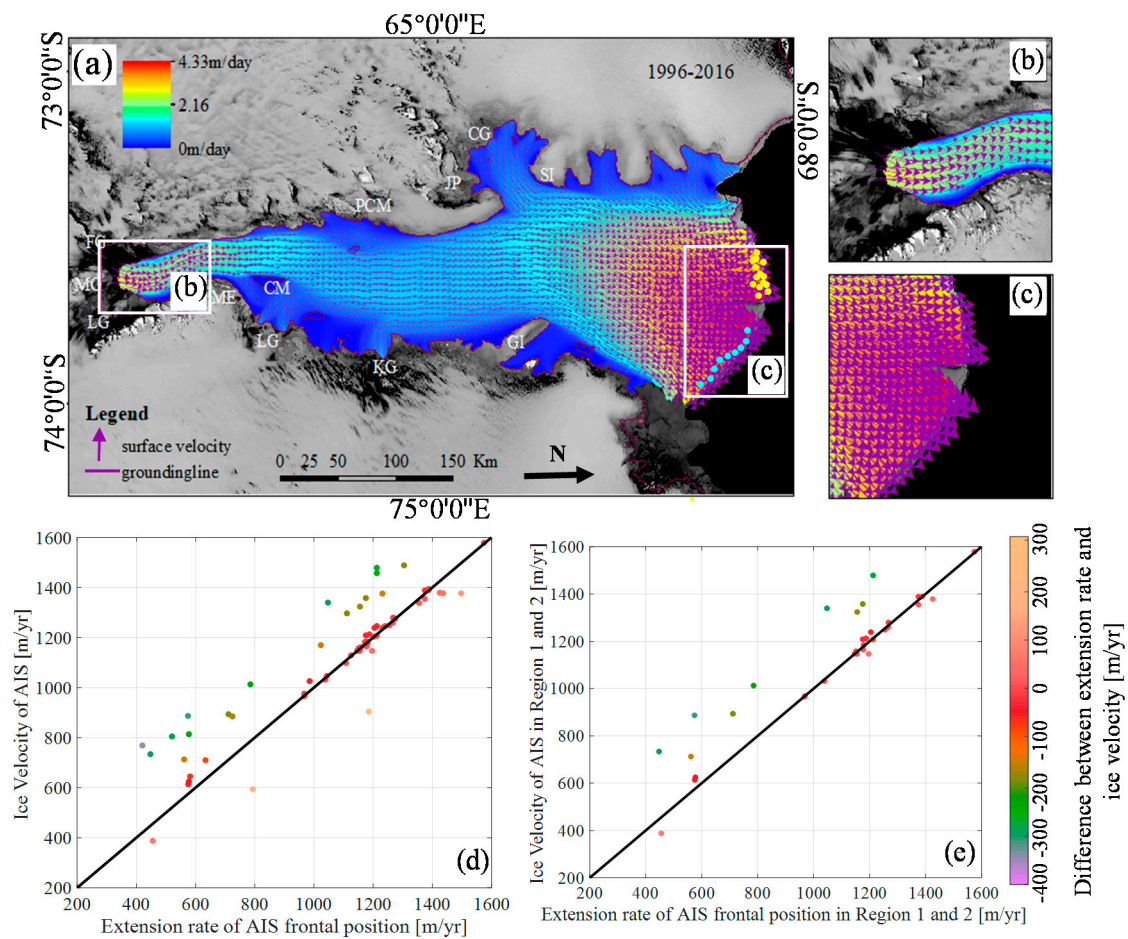


**Figure 10.** Correlation analysis between the frontal extension rate of the AIS and the MEaSUREs ice velocity product. The relation of ice velocity and the extension rate using the scatter plot by the extension rate and MEaSUREs ice velocity products. (a) MEaSURE ice velocity product; (b) ice velocity at the intersection of Lambert Glacier (LG), Fisher Glacier (FG), and Mrellor Glacier (MG); (c) ice velocity in the front of AIS; (d) scatter plot of the extension rate in the front of AIS and MEaSUREs ice velocity product (yellow and light blue points); (e) scatter plot of the extended distance at the frontal position of the D28 disintegration area and MEaSUREs ice velocity product (yellow points).

#### 4. Conclusions

The calving and expansion of ice shelves have significant impacts on ice sheet instability and sea-level rise. As the third-largest ice shelf in Antarctica, the dynamic AIS is of great importance for ice shelf monitoring. In this study, we generated a time series of the frontal line for the AIS using Sentinel-1 SAR data based on a profile analysis method. This study for the first time performed an automated mapping of Antarctic AIS frontal lines using Sentinel-1 SAR imagery for the period 2015–2021. In detail, we modified an ice shelf detection with SO-CFAR algorithm and profile cumulative method for frontal point detection. The main aim during algorithm development was the spatio-temporal analysis of the advance and retreat of AIS frontal lines as well as to provide complementary mapping products. The proposed algorithm was constructed on 75 Sentinel-1 acquisitions covering AIS and additional 14 Sentinel-1 acquisitions covering the D28 event period. By taking into account surface structure on the ice shelf and floating ice in the frontal area, the SO-CFAR target detection method is used to label the SAR as a binary image with the ice shelf and the background. After morphological filtering, a cumulative value-based frontal

point extraction method is proposed. The time-series results show that since March 2015, the average extension distance of the front position of the AIS is 6.5 km, and the length of the front line has increased by 7.5%. Moreover, during the break-off of the D28 iceberg in September 2019, there was a significant increase in the frontal length of the AIS, and it has been in a steady advanced state since then. While the frontal position of the ice shelf retreated during the D28 breakup, and it has been advancing since then. We examined the stable region without an iceberg calving event and found that the frontal advancing rate slowed significantly after the austral summer. In comparison with MEaSURES ice velocity products, we found that the front expansion rate and ice velocity have a good consistency, and an  $R^2$  is 0.88. Further analysis found that before the AIS ice shelf breaks off, the daily average expansion rate of the east and west sides of the D28 ice was greater than 2 m, which caused the rift on the west side of the central AIS image to increase and eventually lead to the breakup of the iceberg. In the future, a long-time series of ice velocity products could be used for correlation analysis. The results of this study demonstrate the high potential of using Sentinel-1 SAR data for monitoring the dynamics of the AIS frontal position.

**Author Contributions:** Conceptualization, T.Z., X.C. and Y.Z.; methodology, T.Z.; software, Y.Z.; validation, T.Z. and Y.Z.; formal analysis, all authors; original draft preparation, T.Z.; review and editing, all authors. All authors have read and agreed to the published version of the manuscript.

**Funding:** This work was supported by the National Key Research and Development Program of China under Grant 2017YFA0603104; the National Natural Science Foundation of China (No. 41801266, 41901275, 41776186, and 41531069); and the China Postdoctoral Science Foundation (No. 2017M612512 and 2018M632922), and LIESMARS special research funding.

**Institutional Review Board Statement:** Not applicable.

**Informed Consent Statement:** Not applicable.

**Data Availability Statement:** The Sentinel-1 SAR data can be downloaded from the ESA Scientific Data Hub (<https://scihub.copernicus.eu/>). The MEaSURES ice velocity product is acquired from the National Snow and Ice Data Center (<https://nsidc.org/data>).

**Conflicts of Interest:** The authors declare no conflict of interest.

## References

- Porter-Smith, R.; McKinlay, J.; Fraser, A.D.; Massom, R.A. Coastal complexity of the Antarctic continent. *Earth Syst. Sci. Data* **2021**, *13*, 3103–3114. [[CrossRef](#)]
- Walker, C.C.; Becker, M.K.; Fricker, H.A. A High Resolution, Three-Dimensional View of the D-28 Calving Event from Amery Ice Shelf with ICESat-2 and Satellite Imagery. *Geophys. Res. Lett.* **2021**, *48*, e2020GL091200. [[CrossRef](#)]
- Walker, C.C.; Bassis, J.N.; Fricker, H.A.; Czerwinski, R.J. Structural and environmental controls on Antarctic ice shelf rift propagation inferred from satellite monitoring. *J. Geophys. Res. Earth Surf.* **2013**, *118*, 2354–2364. [[CrossRef](#)]
- Walker, C.C.; Bassis, J.N.; Fricker, H.A.; Czerwinski, R.J. Observations of interannual and spatial variability in rift propagation in the Amery Ice Shelf, Antarctica, 2002–2014. *J. Glaciol.* **2015**, *61*, 243–252. [[CrossRef](#)]
- Tong, X.; Liu, S.; Li, R.; Xie, H.; Liu, S.; Qiao, G. Multi-track extraction of two-dimensional surface velocity by the combined use of differential and multiple-aperture InSAR in the Amery Ice Shelf, East Antarctica. *Remote Sens. Environ.* **2018**, *204*, 122–137. [[CrossRef](#)]
- Pittard, M.L.; Roberts, J.L.; Warner, R.C.; Galton-Fenzi, B.K.; Watson, C.S.; Coleman, R. Flow of the Amery Ice Shelf and its tributary glaciers. In Proceedings of the 18th Australasian Fluid Mechanics Conference, AFMC 2012, Launceston, Australia, 3–7 December 2012; pp. 18–21.
- Young, N.W.; Hyland, G. Velocity and strain rates derived from InSAR analysis over the Amery Ice Shelf, East Antarctica. *Ann. Glaciol.* **2002**, *34*, 228–234. [[CrossRef](#)]
- Köhler, A.; Nuth, C.; Kohler, J.; Berthier, E.; Weidle, C.; Schweitzer, J. A 15 year record of frontal glacier ablation rates estimated from seismic data. *Geophys. Res. Lett.* **2016**, *43*, 12155–12164. [[CrossRef](#)]
- Fricker, H.A.; Young, N.W.; Allison, I.; Coleman, R. Iceberg calving from the Amery Ice Shelf, East Antarctica. *Ann. Glaciol.* **2002**, *34*, 241–246. [[CrossRef](#)]
- Glasser, N.F.; Scambos, T.A. A structural glaciological analysis of the 2002 Larsen B ice-shelf collapse. *J. Glaciol.* **2008**, *54*, 3–16. [[CrossRef](#)]
- Rignot, E.; Mouginit, J.; Scheuchl, B.; Van Den Broeke, M.; Van Wessem, M.J.; Morlighem, M. Four decades of Antarctic ice sheet mass balance from 1979–2017. *Proc. Natl. Acad. Sci. USA* **2019**, *116*, 1095–1103. [[CrossRef](#)]

12. Cui, X.; Greenbaum, J.S.; Lang, S.; Zhao, X.; Li, L.; Guo, J.; Sun, B. The Scientific Operations of Snow Eagle 601 in Antarctica in the Past Five Austral Seasons. *Remote Sens.* **2020**, *12*, 2994. [[CrossRef](#)]
13. Kachouie, N.N.; Huybers, P.; Schwartzman, A. Localization of mountain glacier termini in Landsat multi-spectral images. *Pattern Recognit. Lett.* **2013**, *34*, 94–106. [[CrossRef](#)]
14. Bhardwaj, A.; Sam, L.; Singh, S.; Kumar, R. Automated detection and temporal monitoring of crevasses using remote sensing and their implications for glacier dynamics. *Ann. Glaciol.* **2016**, *57*, 81–91. [[CrossRef](#)]
15. Jeong, S.; Howat, I.M.; Bassis, J.N. Accelerated ice shelf rifting and retreat at Pine Island Glacier, West Antarctica. *Geophys. Res. Lett.* **2016**, *43*, 11720–11725. [[CrossRef](#)]
16. Euillades, L.D.; Euillades, P.A.; Riveros, N.C.; Masiokas, M.H.; Ruiz, L.; Pitte, P.; Elefante, S.; Casu, F.; Balbarani, S. Detection of glaciers displacement time-series using SAR. *Remote Sens. Environ.* **2016**, *184*, 188–198. [[CrossRef](#)]
17. Wesche, C.; Jansen, D.; Dierking, W. Calving Fronts of Antarctica: Mapping and Classification. *Remote Sens.* **2013**, *5*, 6305–6322. [[CrossRef](#)]
18. Baumhoer, C.A.; Dietz, A.J.; Kneisel, C.; Kuenzer, C. Automated extraction of antarctic glacier and ice shelf fronts from Sentinel-1 imagery using deep learning. *Remote Sens.* **2019**, *11*, 2529. [[CrossRef](#)]
19. Seale, A.; Christoffersen, P.; Mugford, R.I.; O’Leary, M. Ocean forcing of the Greenland Ice Sheet: Calving fronts and patterns of retreat identified by automatic satellite monitoring of eastern outlet glaciers. *J. Geophys. Res. Earth Surf.* **2011**, *116*, 1847. [[CrossRef](#)]
20. Kumar, A.; Srivastava, A.; Yadav, J.; Mohan, R. Spatio-temporal changes and prediction of Amery ice shelf, east Antarctica: A remote sensing and statistics-based approach. *J. Environ. Manag.* **2020**, *267*, 110648. [[CrossRef](#)]
21. Liu, H.; Jezek, K.C. A complete high-resolution coastline of antarctica extracted from orthorectified radarsat SAR imagery. *Photogramm. Eng. Remote Sens.* **2004**, *70*, 605–616. [[CrossRef](#)]
22. Borstad, C.; Khazendar, A.; Scheuchl, B.; Morlighem, M.; Larour, E.; Rignot, E. A constitutive framework for predicting weakening and reduced buttressing of ice shelves based on observations of the progressive deterioration of the remnant Larsen B Ice Shelf. *Geophys. Res. Lett.* **2016**, *43*, 2027–2035. [[CrossRef](#)]
23. Borstad, C.; McGrath, D.; Pope, A. Fracture propagation and stability of ice shelves governed by ice shelf heterogeneity. *Geophys. Res. Lett.* **2017**, *44*, 4186–4194. [[CrossRef](#)]
24. Rosenau, R.; Scheinert, M.; Dietrich, R. A processing system to monitor Greenland outlet glacier velocity variations at decadal and seasonal time scales utilizing the Landsat imagery. *Remote Sens. Environ.* **2015**, *169*, 1–19. [[CrossRef](#)]
25. Han, L.; Floricioiu, D.; Baessler, M.; Eineder, M. An algorithm for the detection of calving glaciers frontal position from TerraSAR-X imagery. In Proceedings of the International Geoscience and Remote Sensing Symposium (IGARSS), Beijing, China, 10–15 July 2016; pp. 6171–6174. [[CrossRef](#)]
26. Ni, W.; Yan, W.; Wu, J.; Zheng, G.; Lu, Y. Statistical analysis and modeling of TerraSAR-X images for CFAR based target detection. In Proceedings of the International Geoscience and Remote Sensing Symposium (IGARSS), Melbourne, Australia, 21–26 July 2013; pp. 1983–1986. [[CrossRef](#)]
27. Anastassopoulos, V.; Lampropoulos, G.A. Optimal CFAR Detection in Weibull Clutter. *IEEE Trans. Aerosp. Electron. Syst.* **1995**, *31*, 52–64. [[CrossRef](#)]
28. Tao, D.; Doulgeris, A.P.; Brekke, C. A Segmentation-Based CFAR Detection Algorithm Using Truncated Statistics. *IEEE Trans. Geosci. Remote Sens.* **2016**, *54*, 2887–2898. [[CrossRef](#)]
29. Hou, B.; Chen, X.; Jiao, L. Multilayer CFAR detection of ship targets in very high resolution SAR images. *IEEE Geosci. Remote Sens. Lett.* **2015**, *12*, 811–815. [[CrossRef](#)]
30. Lee, I.K.; Shamsoddini, A.; Li, X.; Trinder, J.C.; Li, Z. Extracting hurricane eye morphology from spaceborne SAR images using morphological analysis. *ISPRS J. Photogramm. Remote Sens.* **2016**, *117*, 115–125. [[CrossRef](#)]
31. Modava, M.; Akbarizadeh, G. Coastline extraction from SAR images using spatial fuzzy clustering and the active contour method. *Int. J. Remote Sens.* **2017**, *38*, 355–370. [[CrossRef](#)]
32. Perron, J.T.; Royden, L. An integral approach to bedrock river profile analysis. *Earth Surf. Process. Landf.* **2013**, *38*, 570–576. [[CrossRef](#)]
33. Gao, G.; Liu, L.; Zhao, L.; Shi, G.; Kuang, G. An adaptive and fast CFAR algorithm based on automatic censoring for target detection in high-resolution SAR images. *IEEE Trans. Geosci. Remote Sens.* **2009**, *47*, 1685–1697. [[CrossRef](#)]
34. Di Bisceglie, M.; Galdi, C. CFAR detection of extended objects in high-resolution SAR images. *IEEE Trans. Geosci. Remote Sens.* **2005**, *43*, 833–843. [[CrossRef](#)]
35. Krylov, V.A.; Moser, G.; Serpico, S.B.; Zerubia, J. On the method of logarithmic cumulants for parametric probability density function estimation. *IEEE Trans. Image Process.* **2013**, *22*, 3791–3806. [[CrossRef](#)]
36. Gil, J.Y.; Kimmel, R. Efficient dilation, erosion, opening, and closing algorithms. *IEEE Trans. Pattern Anal. Mach. Intell.* **2002**, *24*, 1606–1617. [[CrossRef](#)]
37. Mouginit, J.; Scheuch, B.; Rignot, E. Mapping of ice motion in antarctica using synthetic-aperture radar data. *Remote Sens.* **2012**, *4*, 2753–2767. [[CrossRef](#)]
38. Rignot, E.; Mouginit, J.; Scheuchl, B. Ice flow of the Antarctic ice sheet. *Science* **2011**, *333*, 1427–1430. [[CrossRef](#)]